1   **Microtubule-dependent cell polarity regulates skin-resident macrophage phagocytosis**
2   **and directed cell migration**
3
4   Eric Peterman[1], Andrew Murphy[2], Ian A. Swinburne[3], Sean G. Megason[2], Jeffrey P.
5   Rasmussen[1,4]
6
7   [1] Department of Biology, University of Washington, Seattle, Washington, USA
8   [2] Department of Systems Biology, Harvard Medical School, Boston, Massachusetts,
9   USA
10 [3] Department of Molecular Cell Biology, University of California, Berkeley, California,
11 USA
12 [4] Institute for Stem Cell and Regenerative Medicine, University of Washington, Seattle,
13 Washington, USA
14
15
16 **Correspondence:** rasmuss@uw.edu (J.P.R.) or epeter12@uw.edu (E.P.)
17
18
19 **Condensed title:** Macrophages require microtubules for tissue damage responses
20
21
22 **Keywords:** Microtubule, tissue-resident macrophage, migration, phagocytosis, skin, zebrafish
23
24
25
26
27 **ABSTRACT**
28
29 Immune cells rapidly respond to tissue damage through dynamic properties of the cytoskeleton.
30 How microtubules control immune cell functions during injury responses remains poorly
31 understood. Within skin, tissue-resident macrophages known as Langerhans cells use dynamic
32 dendrites to surveil the epidermis for damage and migrate through a densely packed epithelium
33 to wounds. Here, we use Langerhans cells within the adult zebrafish epidermis as a model to
34 investigate roles for microtubules in immune cell tissue surveillance, phagocytosis, and directed
35 migration. We describe microtubule organization within Langerhans cells, and show that
36 depolymerizing the microtubule cytoskeleton alters dendrite morphology, debris engulfment, and
37 migration efficiency. We find that the microtubule organizing center positions adjacent to
38 engulfed debris and that its position correlates with navigational pathfinding during directed cell
39 migration. Stabilizing microtubules prevents Langerhans cell motility during directed cell
40 migration by impairing navigation around cellular obstacles. Collectively, our work demonstrates
41 requirements for microtubules in the dynamic actions of tissue-resident macrophages during
42 epithelial surveillance and wound repair.

43   **INTRODUCTION**

44

45   Immune cells must respond to wounds quickly to prevent pathogen invasion, clear debris, and

46   promote tissue repair. Rapid responses require that immune cells navigate complex, 3D tissue

47   environments that can range from loosely organized interstitial spaces to densely packed

48   epithelia (Delgado and Lennon-Duménil, 2022). While studies from several systems have begun

49   to reveal mechanisms of interstitial migration (Barros-Becker et al., 2017; Fernandes et al.,

50   2020; Harada et al., 2012; Lämmermann et al., 2009; Nombela-Arrieta et al., 2007; Park et al.,

51   2010; Tabdanov et al., 2021; Weber et al., 2013; Wilson et al., 2013; Yoo et al., 2010),

52   navigation of immune cells within epithelia remains relatively understudied (Alraies et al., 2024;

53   Renkawitz et al., 2019). Understanding how immune cells migrate through solid tissues is

54   relevant to studies of diverse organ and tumor microenvironments.

55

56   The superficial location of skin makes it an excellent model for studying epithelial biology. The

57   epidermis, the outermost layer of skin, contains tightly adherent layers of keratinocytes that form

58   a watertight and mechanical barrier. Interspersed amongst, and confined by, epidermal

59   keratinocytes are various immune cells that must navigate the dense microenvironment (Nestle

60   et al., 2009). Upon skin damage, resident cells quickly mobilize to restore organ function:

61   keratinocytes rearrange to restore the physical barrier, while immune cells migrate to the wound

62   to clear cell debris (Peña and Martin, 2024). Our lab and others recently found that tissue-

63   resident macrophages known as Langerhans cells migrate to sites of damage and promote skin

64   repair (Lin et al., 2019; Peterman et al., 2024; Wang et al., 2024; Wasko et al., 2022).

65   Langerhans cells populate the epidermis and other epithelial tissues such as oral and vaginal

66   mucosa, surveilling tissue and acting as multimodal immune cells capable of emigration to

67   lymph nodes and responding to tissue damage (Brand et al., 2023; Larsen et al., 1990; Lin et

68   al., 2019; Peterman et al., 2024; Vine et al., 2024; Wang et al., 1999b; a, 2024; Wasko et al.,

69   2022). The rapid migration of Langerhans cells to sites of tissue damage makes them an

70   attractive model to study immune cell navigation, but how they pathfind through the confined

71   epidermal microenvironment remains unknown.

72

73   Langerhans cells adopt a ramified morphology in homeostatic skin, and their long and dynamic

74   dendrites facilitate skin surveillance and cell spacing (Kubo et al., 2009; Nishibu et al., 2006;

75   Park et al., 2021). Upon skin damage, Langerhans cells modulate their dendritic morphology to

76   accommodate cell engulfment (Peterman et al., 2024). Arborized and ramified cells such as

77   neurons and microglia, respectively, rely on the actin and microtubule cytoskeletal networks to

78   promote cell functionality. Work by our group and others suggest that actin and actin-regulating

79   networks control Langerhans cell spacing, dendrite dynamics and migration in response to

80   tissue damage (Delgado et al., 2024; Park et al., 2021; Peterman et al., 2024). Microtubules and

81   the microtubule organizing center (MTOC) function prominently during immune cell migration

82   through interstitial microenvironments (Renkawitz et al., 2019; Yoo et al., 2012) and previous

83   studies implicate microtubules in Langerhans cell antigen uptake and presentation (Bacci et al.,

84   1996; Martin et al., 2014), but how microtubules function during immune cell migration through

85   solid epithelia remains an open question.

86

87   Due to its optical clarity, zebrafish skin is an excellent model for studying immune cell motility in
88   a native microenvironment. Along the fish trunk, the epidermis drapes across plate-like scales, a
89   type of dermal appendage **(Figure 1A, B)** (Aman and Parichy, 2024). Similar to other types of
90   vertebrate skin, the adult zebrafish epidermis contains stratified keratinocytes and interspersed
91   immune cells, including T cells and Langerhans cells **(Figure 1B)** (Dee et al., 2016; He et al.,
92   2018; Hui et al., 2017; Lin et al., 2019; Robertson et al., 2023). Previously, we developed an *ex*
93   *vivo* scale explant model that allows for the visualization of Langerhans cell behaviors with high
94   spatiotemporal resolution and acute cytoskeletal manipulation via chemical perturbations
95   (Guerrero et al., 2024; Peterman et al., 2023, 2024). Here, we use this skin explant system in
96   combination with new transgenes to examine the function of microtubules and the MTOC during
97   Langerhans cell skin surveillance and responses to tissue damage.
98
99   **RESULTS AND DISCUSSION**
100
101   ***Microtubule organization in Langerhans cells in homeostatic skin***
102   The zebrafish *mpeg1.1* promoter labels diverse macrophage populations, including Langerhans
103   cells (Ellett et al., 2011; He et al., 2018; Lin et al., 2019; Zhou et al., 2023). To visualize
104   microtubules in Langerhans cells, we created a transgenic line in which the *mpeg1.1* promoter
105   drives expression of the microtubule reporter EMTB-3xGFP (*Tg(mpeg1.1:EMTB-3xGFP)*)
106   (Barros-Becker et al., 2017; Faire et al., 1999). To simultaneously visualize Langerhans cell
107   microtubules and cytoplasm, we crossed this line to *Tg(mpeg1.1:mCherry)* (Ellett et al., 2011),
108   which expresses cytosolic mCherry in Langerhans cells **(Figure 1C, Supplemental Video 1)**.
109   From confocal z-stacks, we identified linear arrays of EMTB-3xGFP signal in at least one
110   dendrite of all Langerhans cells examined (**Figure 1C, arrowheads and 1D,** range: 16.67-100%
111   EMTB-3xGFP+ dendrites/cell; *n*=12 cells). Microtubule organization and polarity is dictated in
112   many cell types by a single microtubule organizing center (MTOC) (Meiring et al., 2020).
113   Previous studies have used EMTB+ foci to identify the MTOC of migrating dendritic cells (Kroll
114   et al., 2023; Renkawitz et al., 2019). While imaging EMTB-3xGFP localization in Langerhans
115   cells, we observed that microtubules appeared to emanate from the brightest point of signal,
116   which localized near the nucleus **(Figure 1C, cyan arrow)**, suggesting this may represent the
117   MTOC**.** As a complimentary approach to MTOC identification, we used the plus-end binding
118   protein EB3 (Stepanova et al., 2003) to label the growing plus-ends of microtubules in
119   Langerhans cells of *Tg(mpeg1.1:mCherry)* adult zebrafish. We found that EB3-GFP+ comets
120   grew from a bright, perinuclear EB3-GFP+ focus **(Figure 1E; Supplemental Video 2)**. Based
121   on these combined data, we concluded that Langerhans cells have a single, perinuclear MTOC,
122   and that microtubules are present in Langerhans cell dendrites.
123
124   To test if microtubules are required to maintain the dendritic morphology of Langerhans cells,
125   we explanted skin and administered nocodazole to depolymerize microtubules **(Figure 1F,G;**
126   **Supplemental Video 3)**. We first confirmed that nocodazole treatment resulted in loss of
127   EMTB-3xGFP signal **(Supplemental Figure 1)**, indicating our reporter faithfully labels
128   microtubules and that nocodazole depolymerized microtubules in our explant system. We next
129   analyzed Langerhans cell morphology using the cytosolic reporter *Tg(mpeg1.1:YFP)* (Roca and
130   Ramakrishnan, 2013) and found that nocodazole treatment significantly decreased Langerhans

131   cell dendrite number compared to vehicle-treated controls **(Figure 1I).** Although average
132   dendrite length was only modestly increased in nocodazole-treated cells **(Figure 1J),** the
133   maximum dendrite length increased significantly **(Figure 1K).** As an alternative measure of
134   dendrite morphology, we used Sholl analysis to measure the number of dendrites crossing
135   concentric circles in increasing 10 micron intervals. Our analysis revealed that microtubule
136   depolymerization significantly increased the range of dendrite lengths **(Figure 1L).** To examine
137   how microtubule stabilization affected Langerhans cell morphology, we also treated scale
138   explants with paclitaxel, a microtubule-stabilizing drug (Schiff and Horwitz, 1980; Schiff et al.,
139   1979). Treatment of scale explants with paclitaxel did not alter dendrite number or length
140   **(Figure 1H-K).** These data indicate that acute microtubule depolymerization, but not
141   stabilization, alters Langerhans cell dendrite number and length in steady-state conditions.
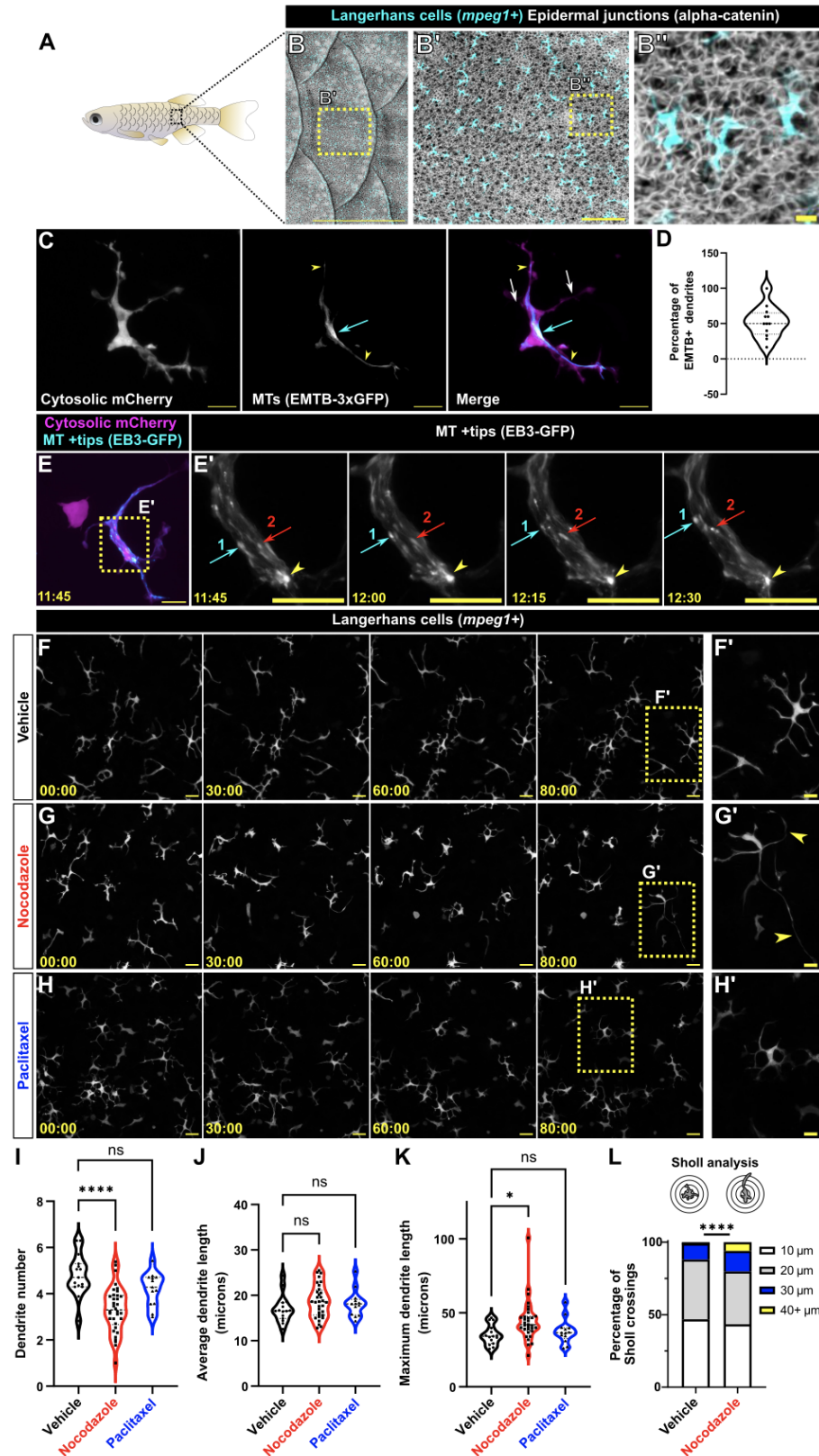142

143
Figure 1. Microtubule depolymerization disrupts Langerhans cell morphology. A. Illustration of adult
144 zebrafish showing overlapping scales along the trunk skin. **B.** Confocal images of adult trunk skin
145

146   expressing reporters for Langerhans cells [Tg(*mpeg1:mCherry)*] and alpha-catenin [*Gt(ctnna1-Citrine)*],
147   which labels epidermal junctions. **C.** Representative image of a Langerhans cell expressing
148   *Tg(mpeg1.1:mCherry;mpeg1.1:EMTB-3xGFP)* showing EMTB-3xGFP+ dendrites (yellow arrowheads),
149   EMTB-3xGFP- dendrites (white arrows), and the presumptive microtubule organizing center (cyan arrow).
150   **D.** Violin plot showing percentage of EMTB+ dendrites *(n* = 12 cells from *N* = 5 scales). **E.** Representative
151   still images from time-lapse confocal microscopy of a *Tg(mpeg1.1:mCherry;mpeg1.1:EB3-GFP)+*
152   Langerhans cell showing the perinuclear focus of EB3 signal (yellow arrowhead). Yellow box in left panel
153   denotes region magnified in the panels at right. Red and cyan arrows track individual growing
154   microtubules. **F-H.** Representative still images from time-lapse confocal microscopy depicting effects of
155   vehicle **(F),** nocodazole **(G)**, or paclitaxel **(H)** treatment on *Tg(mpeg1.1:YFP)+* Langerhans cell
156   morphology. Yellow arrowheads in **(G)** indicate elongated dendrites. **I-K.** Violin plots showing average
157   dendrite number **(I)**, average dendrite length **(J)**, or maximum dendrite length **(K)** through 80 minutes of
158   vehicle, nocodazole, or paclitaxel treatment. *n* = 15 cells tracked from *N* = 3 scales for vehicle control, *n* =
159   27 cells tracked from *N* = 5 scales for nocodazole, *n* = 13 cells tracked from *N* = 6 scales for paclitaxel. **L.**
160   Sholl analysis of dendrite lengths in vehicle- and nocodazole-treated conditions. *n* = 698 dendrites
161   tracked in 14 cells from *N* = 3 scales for vehicle control and n = 476 dendrites tracked in 11 cells from *N* =
162   3 scales for nocodazole. Statistical significance in **(I, J, K)** was determined using Mann-Whitney U test,
163   statistical significance in **(L)** was determined using a chi-squared test with the raw number of dendrites. *
164   = *p* < 0.05, **** = *p* < 0.0001. Timestamps denote mm:ss. Scale bars, 1 mm **(B),** 100 μm **(B'),** 10 μm **(B'',**
165   **C, E, F'-H')**, 20 μm **(F-H).**

166
167

168   ***The perinuclear microtubule organizing center rapidly localizes to sites of debris***
169   ***engulfment***
170   We next questioned if the microtubule cytoskeleton was important for debris engulfment by
171   Langerhans cells. We began by measuring MTOC motility during steady-state conditions and
172   observed that the brightest EMTB-3xGFP focus per cell (hereafter referred to as the MTOC)
173   moved an average of 1.39 microns/minute in the absence of stimulus **(Figure 2A,B;**
174   **Supplemental Video 1).** Next, we tracked Langerhans cell engulfment of laser-damaged single
175   keratinocytes as previously described **(Figure 2C)** (Guerrero et al., 2024; Peterman et al.,
176   2024). Consistent with observations in microglia (Möller et al., 2022), we found that the
177   Langerhans cell MTOC relocalized to the site of debris contact after laser ablation **(Figure**
178   **2D,E; Supplemental Video 4).** When we quantified the distance that the MTOC traveled 5
179   minutes prior to ablation and 5 minutes prior to engulfment, we found that the MTOC traveled
180   further distances following Langerhans cell activation **(Figure 2F)**. Additionally, we found that
181   MTOC speed was faster after laser ablation (average of 1.83 microns/minutes) compared to
182   pre-ablation (average of 1.26 microns/minute) **(Figure 2G)**. Altogether, these data show that
183   Langerhans cell MTOC motility increases after nearby cellular damage and that the MTOC
184   relocalizes proximal to debris during engulfment.
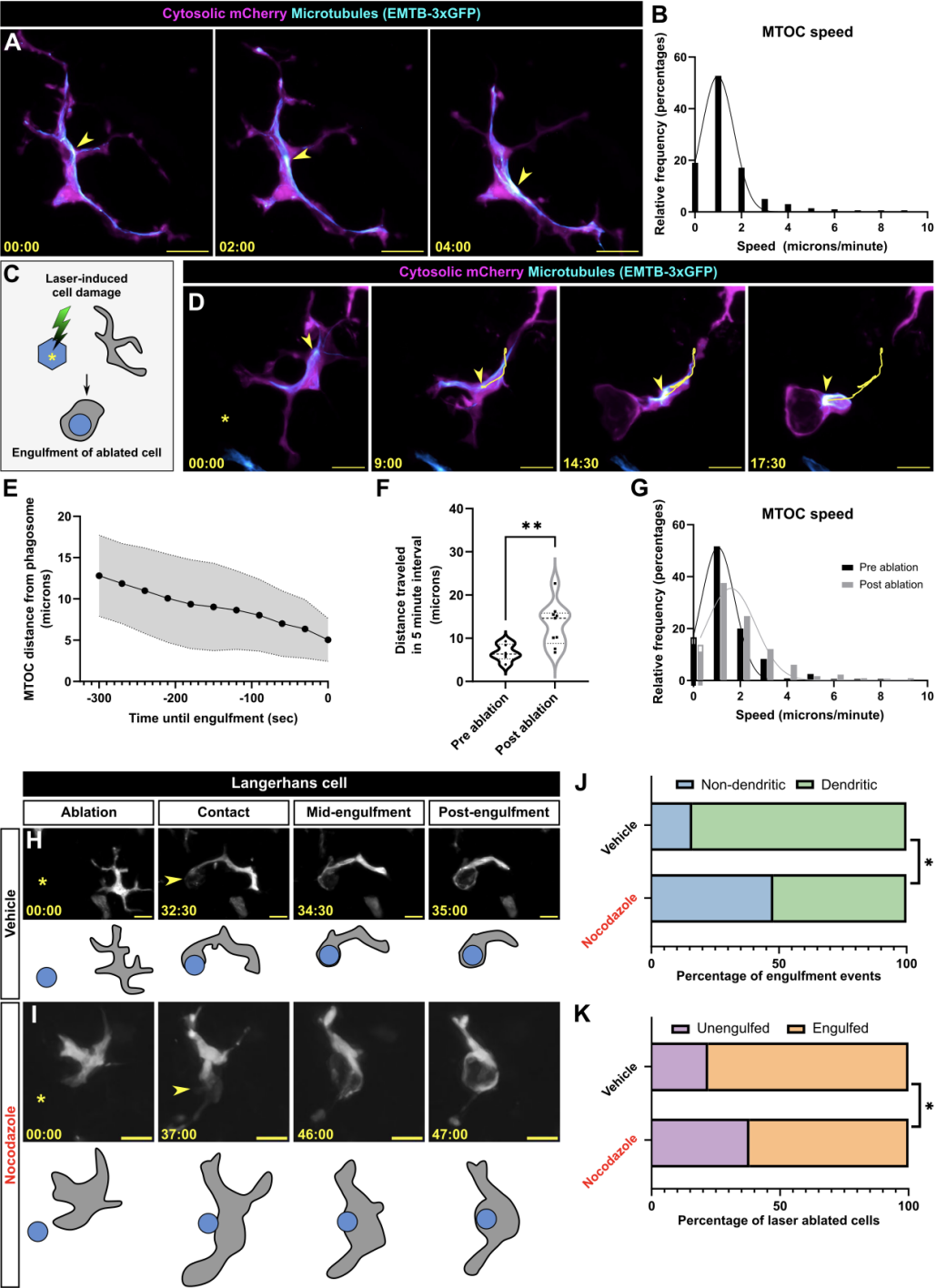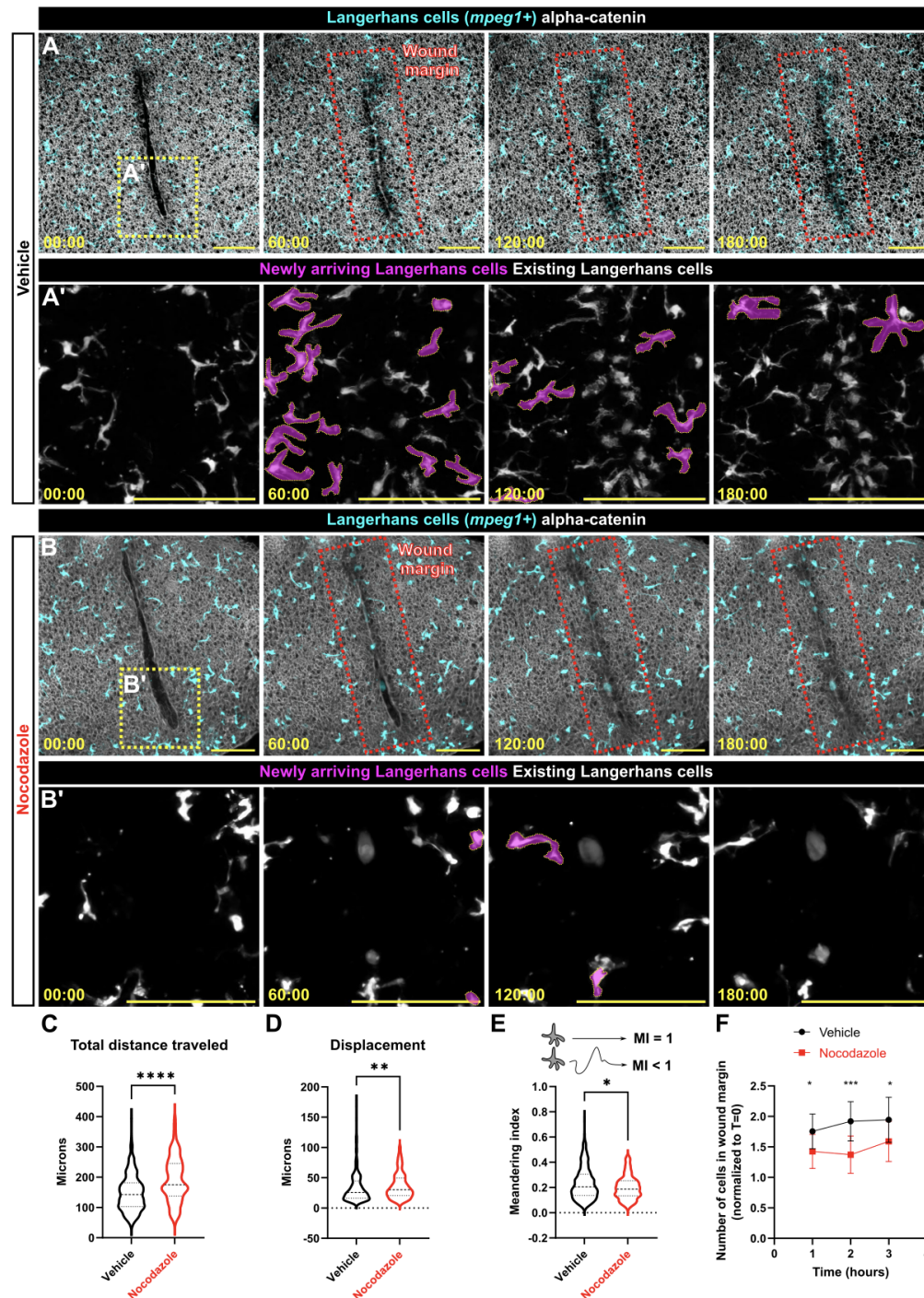185
186
187

188
189
190 **Figure 2. MTOC dynamics and microtubule requirements during debris engulfment.**
191 **A.** Representative still images from time-lapse confocal microscopy of a
192 *Tg(mpeg1.1:mCherry;mpeg1.1:EMTB-3xGFP)+* Langerhans cell showing MTOC (yellow arrowhead)
193 movement in steady-state conditions. **B.** Histogram showing the frequency distribution of MTOC speed in
194 steady-state conditions, n = 10 cells tracked from N = 5 scales. **C.** Schematic of laser-induced
195 keratinocyte (blue) damage and subsequent Langerhans cell engulfment. **D.** Representative still images
196 from time-lapse confocal microscopy showing MTOC (yellow arrowhead) motility preceding engulfment of

197   debris generated by keratinocyte laser ablation. Yellow trace indicates the MTOC track over time. Yellow
198   asterisk indicates the site of laser ablation. **E.** Quantification of the distance between the MTOC and
199   phagosome in the 5 minutes prior to debris engulfment, n = 9 cells tracked from N = 4 scales. Gray
200   shading represents a 95% confidence interval. **F.** Violin plot of the total distance traveled by the MTOC 5
201   minutes prior to keratinocyte laser ablation and 5 minutes prior to keratinocyte engulfment, n = 6 cells
202   tracked in pre ablation, n = 9 cells tracked in post ablation from N = 4 scales. **G.** Histogram of the
203   frequency distribution of MTOC speed 5 minutes prior to keratinocyte laser ablation and 5 minutes prior to
204   keratinocyte engulfment , n = 6 cells tracked in pre ablation, n = 9 cells tracked in post ablation from N = 4
205   scales. **H,I.** Representative still images from time-lapse confocal microscopy of vehicle- **(H)** or
206   nocodazole-treated **(I)** *Tg(mpeg1.1:YFP)+* Langerhans cells showing engulfment of debris. Yellow
207   asterisk indicates the site of laser ablation. Yellow arrowhead indicates site of first contact between the
208   Langerhans cell and laser-damaged cell. **J.** Quantification of engulfment modality used to engulf debris, n
209   = 25 engulfment events tracked from N = 3 individual experiments for vehicle control, n = 23 ablation
210   events tracked from N = 3 individual experiments for nocodazole. **K.** Quantification of successful
211   keratinocyte debris engulfment following addition of vehicle or nocodazole, n = 30 ablated cells tracked
212   from N = 3 individual experiments for vehicle control, n = 26 ablated cells tracked from N = 3 individual
213   experiments for nocodazole. Statistical significance in **(F)** was determined using a Mann-Whitney U test.
214   A Kolmogorov-Smirnov test was used in **(G)** and revealed no significant difference. Fisher's exact test
215   was used to determine significance in **(J,K)** by using the raw counts of engulfment events**.** Traces in
216   frequency distribution graphs **(B)** and **(G)** are Gaussian fits. * = p < 0.05, ** = p < 0.01. Timestamps
217   denote mm:ss. Scale bars, 10 µm **(A,D,H,I)**.
218
219   ***Dendrite-mediated engulfment of debris requires the microtubule cytoskeleton***
220   Our results indicate that microtubule depolymerization alters Langerhans cell dendrite
221   morphology and that the MTOC polarizes towards cell debris after laser ablation. This led us to
222   hypothesize that microtubules may be required for debris engulfment. To test this, we used our
223   laser ablation paradigm in combination with vehicle or nocodazole treatment and tracked debris
224   engulfment. In vehicle-treated conditions, we observed two modes of debris engulfment by
225   Langerhans cells. The predominant modality involved Langerhans cells contacting debris with a
226   single, long dendrite, while simultaneously retracting distal dendrites prior to debris engulfment
227   **(Figure 2H,J;** 84% of events**; Supplemental Video 5)**. Alternatively, Langerhans cells adopted
228   a non-dendritic modality in which the entire cell migrated and repositioned itself next to the
229   debris, which was then engulfed at the cell body **(Figure 2J;** 16% of events**)**. By contrast, in
230   nocodazole-treated conditions, Langerhans cells exhibited increased usage of the motility-
231   based engulfment modality **(Figure 2I,J)** and a decrease in the ability to engulf debris **(Figure
232   2K)**. These results suggest that microtubules are partly responsible for dendrite-mediated
233   engulfment and overall engulfment success of damaged keratinocytes.
234
235

Figure 3. Langerhans cell migration to scratch wounds requires microtubules. A,B. Langerhans cell migration to epidermal scratch in vehicle- **(A)** or nocodazole-treated **(B)** conditions. Yellow boxes in first frames of **(A, B)** indicate insets in A', and B', red boxes in frames 2-4 indicate the wound margin ROI corresponding to cell counts in **(F)**. Newly arriving Langerhans cells are pseudocolored magenta in **A', B'**. **C-E.** Violin plots showing total distance traveled **(C)**, displacement **(D)**, or the meandering index **(E)** of *mpeg1+* cells over 3 hours in response to epidermal scratch in vehicle- or nocodazole-treated conditions, n = 325 cells from N = 11 skin explants tracked in vehicle conditions, n = 181 cells from N = 10 skin

245 explants tracked in nocodazole conditions. **F.** Quantification of the normalized number of *mpeg1+* cells in
246 the wound margin in vehicle- or nocodazole-treated conditions, *N* = 13 skin explants for vehicle
247 conditions, *N* = 12 skin explants for nocodazole conditions. Mann Whitney U tests were used to determine
248 significance in **(C-E),** two-way ANOVA followed by Bonferroni post-test was used to determine
249 significance in **(F).** * = $p < 0.05$, ** = $p < 0.01$, *** = $p < 0.001$, **** = $p < 0.0001$. Timestamps denote
250 mm:ss. Scale bars, 100 μm **(A, B).**
251
252 ***Efficient directed cell migration requires the microtubule cytoskeleton***
253 In addition to their function in regulating phagocytosis, microtubules and the MTOC play pivotal
254 roles in immune cell migration (Etienne-Manneville, 2013). Previous work demonstrated that
255 murine and zebrafish Langerhans cells migrate to tissue wounds generated by punch biopsy or
256 mechanical scratch, respectively (Wasko et al., 2022; Peterman et al., 2024; Lin et al., 2019),
257 but the underlying mechanisms that promote migration remain unknown. To ask if Langerhans
258 cells require microtubules for directional migration, we pretreated explanted scales with vehicle
259 or nocodazole, introduced an epidermal scratch, and imaged cell migration over 3 hours **(Figure**
260 **3A,B; Supplemental Video 6)**. Compared to vehicle-treated controls, nocodazole-treated cells
261 migrated with a significantly larger total distance traveled and displacement **(Figure 3C,D)**. As a
262 measure of the efficiency of migration, we calculated the meandering index (defined as the ratio
263 of displacement to total distance traveled) and found that Langerhans cells had a smaller
264 meandering index, indicating the cells did not migrate as directly toward the wound **(Figure 3E)**.
265 Confirming this, we observed significantly fewer nocodazole-treated cells in the wound margin
266 **(Figure 3F)**. Altogether, these data indicate that microtubule depolymerization causes increased
267 Langerhans cell motility, but with less directionality, leading to reduced cell accumulation at sites
268 of tissue damage.
269
270 ***Microtubule depolymerization alters actin distribution in migrating Langerhans cells***
271 We next asked how microtubules promote efficient Langerhans cell migration to wounds.
272 Previous works indicate multiple modes of crosstalk between the microtubule and actin
273 cytoskeletons (Dogterom and Koenderink, 2019). One such mechanism involves sequestration
274 of the RhoA activator GEF-H1/ARHGEF2 through binding to microtubules (Heck et al., 2012;
275 Kashyap et al., 2019; Krendel et al., 2002). Microtubule depolymerization releases GEF-H1 from
276 the microtubule lattice, leading to RhoA activation and subsequent changes in cell shape and
277 actin distribution. Notably, our previous work suggests that a RhoA/Rho-associated kinase
278 (ROCK)/myosin pathway promotes Langerhans cell migration to tissue wounds (Peterman et
279 al., 2024). We hypothesized that Langerhans cell microtubule depolymerization alters RhoA
280 activity and actin distribution, thereby disrupting migration towards wounds. To visualize F-actin
281 in Langerhans cells and epidermal wounds, we used skin explants from *Tg(mpeg1.1:Lifeact-*
282 *mRuby)* fish (Peterman et al., 2024). After explant, we pretreated scales with vehicle or
283 nocodazole and scratched the epidermis. We followed individual cells as they migrated towards
284 the wound and quantified Lifeact-mRuby ratios in the leading and trailing halves of migrating
285 Langerhans cells. In vehicle-treated cells, we found roughly equal amounts of Lifeact-mRuby in
286 the leading and trailing halves **(Figure 4A, A', D)**. By contrast, nocodazole-treated cells
287 contained an enrichment of Lifeact-mRuby in the trailing half, consistent with the idea
288 depolymerizing microtubules increases RhoA activity at the rear of the cell **(Figure 4B, B'**
289 (arrowheads)**, D)**. To inhibit a prominent downstream target of RhoA, we next used the ROCK

290   inhibitor Y-27632 (Ishizaki et al., 2000), which we previously used to modulate Langerhans cell
291   damage responses (Peterman et al., 2024). The addition of Y-27632 to nocodazole-treated
292   explants restored Lifeact-mRuby ratios to near-control levels **(Figure 4C, C', D)**. These data
293   suggest that depolymerization of microtubules alters actin distribution through a ROCK-
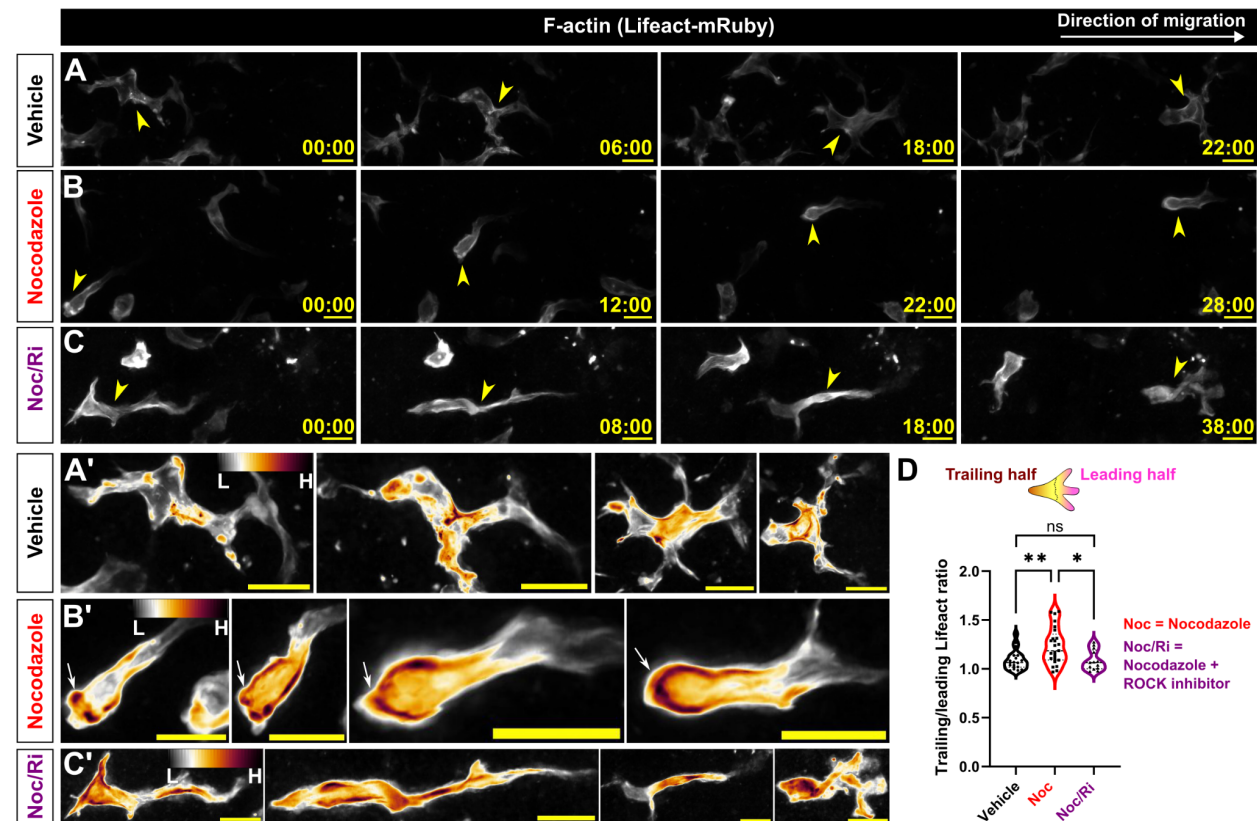294   dependent mechanism in migrating cells and is one plausible cause for altered cell migration.
295

296
297   **Figure 4. Microtubule depolymerization increases F-actin levels in a ROCK-dependent manner in**
298   **the trailing halves of migrating Langerhans cells. A-C.** Stills from time-lapse confocal microscopy
299   showing migrating *Tg(mpeg1.1:Lifeact-mRuby)+* Langerhans cells treated with vehicle **(A)**, nocodazole
300   **(B)**, or nocodazole+Y-27632 (Noc/Ri) **(C)**. Magnified insets in **(A'-C')** are false-colored to show Lifeact-
301   mRuby levels. Arrowheads in **(A-C)** indicate migrating cell, arrows in **(B')** indicate increased Lifeact-
302   mRuby levels in the trailing half of a nocodazole-treated cell. **D.** Violin plot quantifying the ratio of Lifeact-
303   mRuby at the trailing and leading halves (see Materials and Methods for analysis detail), $n = 20$ cells
304   tracked from $N = 3$ individual experiments in vehicle conditions, $n = 25$ cells tracked from $N = 4$ individual
305   experiments in nocodazole-treated conditions, $n = 13$ cells tracked from $N = 6$ individual experiments in
306   nocodazole+ROCK inhibitor-treated conditions. Significance was determined using one-way ANOVA
307   followed by Bonferroni post-test. * = $p < 0.05$, ** = $p < 0.01$. Timestamps denote mm:ss. Scale bars, 10
308   µm **(A-C)**.
309

310   ***Pathfinding during directional cell migration involves MTOC decision-making***
311   While imaging Langerhans cell migration to epidermal wounds, we observed that Langerhans
312   cell bodies would often transiently pause while their dendrites continued to extend and retract
313   **(Figure 5A-A''')**. Close examination of this phenomenon revealed that keratinocytes appeared
314   to impede Langerhans cell migration to the wound.

315

316 A primary role for microtubules and the MTOC in immune cell function is dictating cell polarity
317 and directionality of migration (Kopf et al., 2020; Kroll et al., 2023; Renkawitz et al., 2019). This
318 is accomplished by positioning microtubule-associated proteins including vesicle cargo, motors
319 and focal adhesions. Certain cell types, such as dendritic cells, often exhibit a nucleus-first
320 mode of migration, while neutrophils can exhibit either MTOC- or nucleus-first migration
321 (Etienne-Manneville, 2013). Therefore, we first asked how the MTOC was positioned during
322 directional migration and whether or not its position corresponded to pathfinding decisions. To
323 facilitate imaging nuclear positioning of all epidermal cells, we generated a transgenic line in
324 which the quasi-ubiquitous *beta-actin2* (*actb2*) promoter (Kobayashi et al., 2014) drives
325 expression of the histone H2B fused to a tandem repeat of the red fluorescent protein mScarlet
326 (Bindels et al., 2017) [*Tg(actb2:H2B-2x-mScarlet)*]. By scratching skin explants from
327 *Tg(mpeg1.1:EMTB-3xGFP;actb2:H2B-2x-mScarlet)* fish, we could track the Langerhans cell
328 MTOC and nucleus as the cell migrated towards the wound **(Figure 5B; Supplemental Video
329 7)**. As Langerhans cells migrated towards the wound, we observed that cells would often
330 encounter surrounding nuclei and pause **(Figure 5B')**. While paused, Langerhans cell dendrites
331 explored the space beyond the keratinocyte obstacle. In 21/25 instances, the MTOC preceded
332 the nucleus past the obstacle keratinocyte **(Figure 5B')**.

333

334 Prior studies found that paclitaxel-mediated microtubule stabilization can inhibit cell migration
335 (Ganguly et al., 2011; Wang et al., 2019) and centriole motility (Ching et al., 2022). To
336 determine the effects of microtubule stabilization on Langerhans cell migration, we performed
337 the scratch injury assay in the presence of paclitaxel or vehicle control. Using skin explants from
338 *Tg(mpeg1.1:EMTB-3xGFP;actb2:H2B-2x-mScarlet)* fish and observing MTOC position as a
339 proxy for successful navigation, we examined how cells and microtubules behaved after
340 paclitaxel treatment. Vehicle-treated Langerhans cells successfully navigated past obstacle cells
341 76% of the time with an average navigation time of 675 s **(Figure 5C,F,G; Supplemental Video
342 8)**. By contrast, paclitaxel-treated Langerhans cells failed obstacle navigation 77% of the time
343 **(Figure 5D-F)**. When paclitaxel-treated cells managed to successfully navigate past their
344 obstacle, navigation times were significantly longer compared to control cells, averaging 2175 s
345 **(Figure 5G)**. To observe possible outcomes from this inability to navigate the epidermis, we
346 tracked Langerhans cell behaviors as they attempted to enter the wound margin using skin
347 explants from *Tg(mpeg1.1:YFP;actb2:H2B-2x-mScarlet)* fish. After 2 hours in control conditions,
348 we observed a subset of Langerhans cells had entered the closing wound and engulfed debris
349 (**Figure 5H**, arrows, **Figure 5J,** average of 20% of cells per wound margin ROI). Less
350 frequently, we noted Langerhans cells on the wound margin did not enter the recovering wound
351 but instead projected an extended dendrite into the region (**Figure 5H,** arrowhead, **Figure 5J,**
352 average of 4.7% of cells per wound margin ROI). In paclitaxel-treated conditions, Langerhans
353 cells entered the wound margin to engulf debris at a significantly lower rate, and we observed a
354 moderate increase in the number of cells that probed the wound with extended dendrites
355 **(Figure 5H,** arrowheads, **Figure 5J)**. Together, these results suggest that Langerhans cells use
356 MTOC positioning to aid in circumventing cellular obstacles during migration and that stabilizing
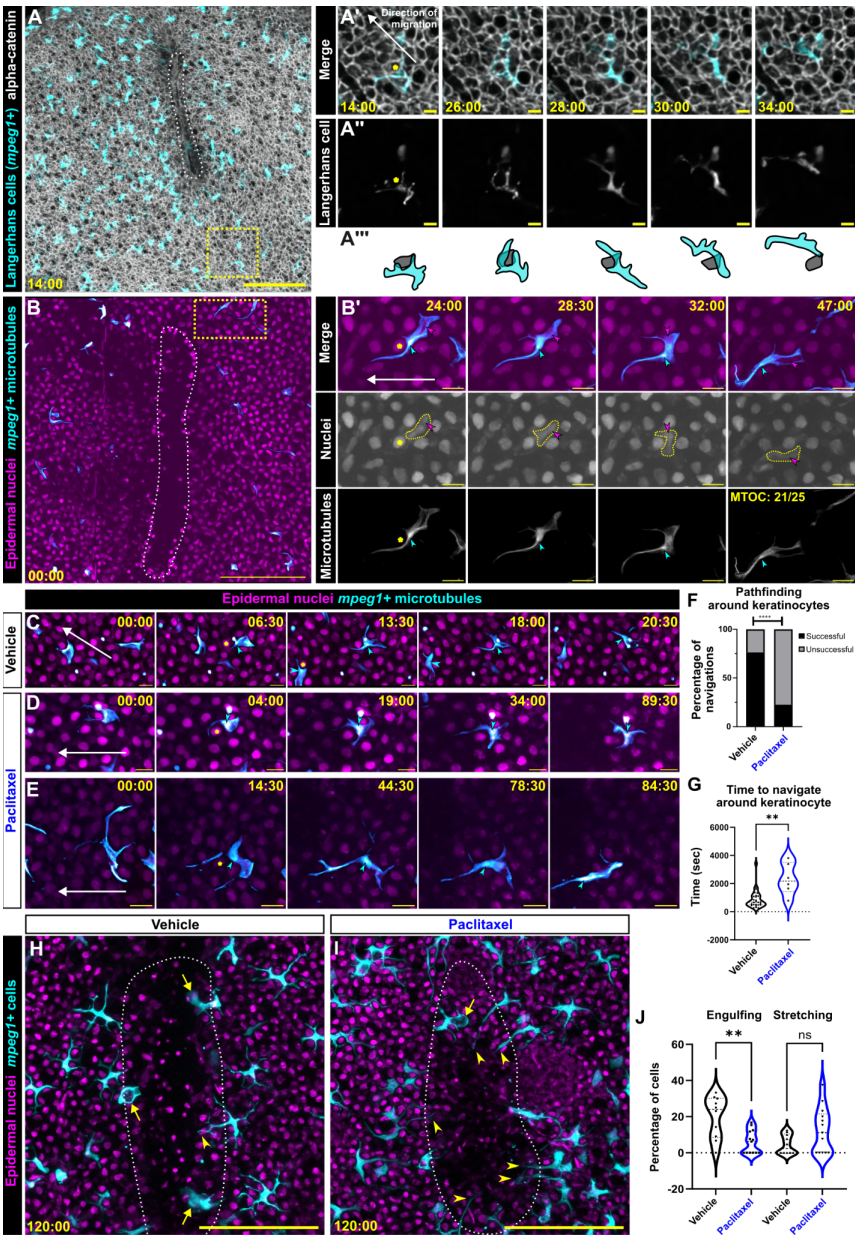357 microtubules inhibits navigational pathfinding to wounds.

358

359
360

361
362

Figure 5. MTOC motility correlates with navigational pathfinding towards large epidermal wounds.
A. Maximum intensity projection from time-lapse confocal microscopy of Tg(*mpeg1:mCherry*);*Gt(ctnna1-Citrine)* skin explant. White dotted outline indicates epidermal scratch. Yellow box in **(A)** is magnified in **(A',A'')** insets as single *z*-slices. Yellow asterisk indicates obstacle keratinocyte. **B.** Representative still images from time-lapse confocal microscopy of *Tg(actb2:H2B-2x-mScarlet;mpeg1.1:EMTB-3xGFP)* skin explants. White dotted outline indicates epidermal scratch. Yellow box in **(B)** is magnified in **(B')** insets. Yellow asterisk indicates obstacle nucleus, cyan arrowhead indicates MTOC, magenta arrowhead indicates Langerhans cell nucleus. 21 out of 25 (84%) of cells exhibit MTOC-first phenotype from *N* = 3 individual experiments. **C.** Representative still images from time-lapse confocal microscopy of vehicle-treated *Tg(actb2:H2B-2x-mScarlet;mpeg1.1:EMTB-3xGFP)*+ Langerhans cells navigating around

373 obstacle keratinocytes towards a wound. **D, E.** Representative still images from time-lapse confocal
374 microscopy of paclitaxel-treated *Tg(actb2:H2B-2x-mScarlet;mpeg1.1:EMTB-3xGFP)+* Langerhans cells
375 attempting to navigate around obstacle keratinocytes towards a wound. Yellow asterisks denote obstacle
376 keratinocyte, cyan arrowhead denote MTOC. **F.** Quantification of navigation attempts in vehicle-treated
377 and taxol-treated conditions, *n* = 38 attempts tracked from *N* = 3 individual experiments in vehicle
378 conditions, *n* = 31 attempts tracked from *N* = 3 individual experiments in taxol conditions. **G.** Violin plots
379 showing the length of time required to navigate around keratinocyte, *n* = 26 cells tracked from *N* = 3
380 individual experiments in vehicle conditions, *n* = 6 cells tracked from *N* = 3 individual experiments in taxol
381 conditions. **H, I.** Representative still images from time-lapse confocal microscopy of *Tg(actb2:H2B-2x-*
382 *mScarlet;mpeg1.1:YFP)* skin explants treated with vehicle **(H)** or paclitaxel **(I).** Yellow dotted line indicates
383 wound**,** asterisks indicate phagocytic cells in wound margin, arrowheads indicate cells with stretched
384 dendrites. **J.** Violin plots showing the percentage of cells exhibiting phagocytosis or stretching after 2
385 hours, *n* = 299 cells counted from *N* = 10 scales in vehicle conditions, *n* = 128 cells counted from *N* = 13
386 scales. Fisher's exact test was used to determine significance in **(F)** by using the raw numbers of
387 successful and unsuccessful navigations**.** Mann Whitney U test was used to determine significance in **(G)**.
388 One-way ANOVA followed by Bonferroni post-test was used to determine significance in **(J).** ** = *p* <
389 0.01, **** = *p* < 0.0001. Timestamps denote mm:ss. Scale bars, 10 μm **(B'-E)**, 100 μm **(B, H, I)**.
390
391 ***Summary: Microtubules dictate immune responses to tissue damage***
392 How immune cells dynamically and rapidly navigate densely packed epithelia to respond to
393 injury remains largely unknown. Here, we use scale explants from adult zebrafish skin as a
394 tractable model to examine tissue-resident macrophage behaviors within a native epithelial
395 microenvironment and apply acute chemical perturbations to modulate the microtubule
396 cytoskeleton. We show that microtubule depolymerization alters Langerhans cell morphology,
397 including dendrite number and length. We find that the MTOC rapidly moves towards the
398 phagosome during debris engulfment and that microtubules are partially required for efficient
399 debris engulfment. What functions might the microtubule cytoskeleton play during
400 phagocytosis? Using cultured macrophages, (2007; Athlin et al., 1986; Walter et al., 1980)
401 found that the MTOC reorients during phagocytosis of antibody-coated beads and red blood
402 cells and that microtubules were strictly required for engulfment. The authors posited that the
403 MTOC can increase interactions between the Golgi apparatus and the phagosome, which may
404 facilitate subsequent cross-presentation events between the phagocyte and other immune cells
405 (Eng et al., 2007). By contrast, Möller et al., (2022) found that depolymerization of microtubules
406 changed how zebrafish microglia encounter and engulf apoptotic corpses *in vivo*. In the
407 absence of microtubules, microglia relied more heavily on a motility-based engulfment strategy
408 (Möller et al., 2022), similar to our own observations **(Figure 2H-J)**, highlighting the flexible
409 engulfment abilities of phagocytes within native microenvironments.
410
411 During directed migration to scratch wounds, we found that Langerhans cells frequently paused
412 at sites of keratinocyte contact, which present potential decision points, akin to microfluidic
413 mazes developed to study migration decisions *in vitro* (Ambravaneswaran et al., 2010; Kopf et
414 al., 2020; Kroll et al., 2023; Renkawitz et al., 2018; Tweedy et al., 2020). By imaging
415 Langerhans cell microtubules, we found that MTOC positioning frequently, but not exclusively,
416 correlated with pathfinding during migration. Perturbing microtubule polymerization and stability
417 affected migration efficiency and actin localization. Our data suggest two non-mutually exclusive
418 models in which microtubules and the MTOC promote efficient migration: through the

419   sequestration and release of actin-regulating proteins, and through decision making in
420   directional migration around obstacles. Further dissecting these mechanisms will require
421   developing methodology to specifically manipulate actin-microtubule crosstalk and the MTOC in
422   Langerhans cells.
423
424   Collectively, our work demonstrates requirements for microtubules in steady-state organ
425   surveillance and directed cell migration by tissue-resident macrophages during wound repair.
426   Uncovering the details and regulation of Langerhans cell motility are important not only for
427   understanding responses to tissue injury, but also for how these cells initially seed the skin, and
428   emigrate from the skin to secondary immune organs.
429

442   **Author contributions**
443   Conceptualization: E.P., J.P.R.; Methodology: E.P.; Formal analysis: E.P.; Investigation: E.P.;
444   Resources: E.P., A.M, I.A.S; Writing-original draft: E.P.; Writing-review & editing: E.P., J.P.R.;
445   Visualization: E.P., J.P.R.; Supervision: E.P., S.G.M, J.P.R.; Project administration: E.P., J.P.R.;
446   Funding acquisition: E.P., J.P.R.
447

448   **Declaration of interests**
449   The authors declare no competing interests.
450

451   **MATERIALS AND METHODS**
452

453   *Key resources table*
454

Reagent or Resource	Source	Identifier
Experimental models: Organisms		
Zebrafish: AB	This paper	ZFIN: ZDB-GENO-960809-7
Zebrafish: *Tg(mpeg1.1:mCherry)^{gl23Tg}*	(Ellett et al., 2011)	ZFIN: ZDB-TGCONSTRCT-120117-2

Zebrafish: *Tg(mpeg1.1:YFP)*^{w200Tg}	(Roca and Ramakrishnan, 2013)	ZFIN: ZDB-TGCONSTRCT-130130-3
Zebrafish: *Tg(actb2:h2b-mscarlet-mscarlet)*^{hm63Tg} *(referred to as Tg(actb2:H2B-2x-mScarlet))*	This paper	n/a
Zebrafish: *Tg(mpeg1.1:EMTB-3xGFP)*^{w270Tg}	This paper	n/a
Zebrafish: *Gt(ctnna1-Citrine)*^{ct3aGt}	(Trinh et al., 2011)	ZFIN: ZDB-ALT-111010-23
Zebrafish: *Tg(mpeg1.1:Lifeact-mRuby)*^{w269Tg}	(Peterman et al., 2024)	n/a
Zebrafish: *Tg(actb2:myl12.1-EGFP)*^{e2212Tg}	(Maître et al., 2012)	ZFIN: ZDB-TGCONSTRCT-130108-2
Chemicals, peptides, and recombinant proteins		
L-15 media	Gibco	21083027
Ethyl 3-aminobenzoate methanesulfonate	Millipore Sigma	E10521
DMSO	Acros Organics	295522500
Nocodazole	Millipore Sigma	M1404
Y-27632 2HCL	SelleckChem	S1049
Paclitaxel	Cayman Chemical	10461
Recombinant DNA		
mpeg1.1:EMTB-3xGFP	(Barros-Becker et al., 2017)	n/a
mpeg1.1:EB3-GFP	This paper	n/a
EB3-F 5' GTGCAGGAGACAGCAAAACAGCCACCATGGCCGT 3	This paper	n/a
EB3-R 5' TAGTTCTAGAGGCTCGAGAGTTA	This paper	n/a

CTTGTACAGCTCGTCCATGCCGA GAGTG 3'		
mpeg1.1_V_F 5' TGGACGAGCTGTACAAGTAACTC TCGAGCCTCTAGAACTATAGTGA GT 3'	This paper	n/a
mpeg1.1_V_R 5' ACATTGACGGCCATGGTGGCTGT TTTGCTGTCTCCTGCACTAATG 3'	This paper	n/a
Software and algorithms		
Fiji/ImageJ	(Schindelin et al., 2012)	RRID:SCR_002285
NIS-Elements 5.30	Nikon	RRID:SCR_014329
Prism 9	GraphPad	RRID:SCR_002798

455

Zebrafish husbandry

456

457 Zebrafish were housed at 26-27°C on a 14/10 h light cycle. The strains used are listed in the
458 Key Resources Table. Animals aged 6-18 months of either sex were used in this study. All
459 zebrafish experiments were approved by the Institutional Animal Care and Use Committee at
460 the University of Washington (Protocol #4439-01).

461

Generation of transgenic zebrafish

462

463 To generate *Tg(mpeg1.1:EMTB-3xGFP)*^{w270Tg}*,* a previously published *mpeg1.1:EMTB-3xGFP*
464 plasmid (Barros-Becker et al., 2017) and *tol2* mRNA were injected into AB embryos at the 1-cell
465 stage, and embryos were raised to adulthood. Adults were screened for GFP+ cells in the skin,
466 and GFP+ adults were then outcrossed to wild-type partners. F1 fish were raised to adulthood,
467 where GFP expression was assessed in Langerhans cells to identify a line to propagate for this
468 study.

469

470 To generate *Tg(mpeg1.1:EB3-GFP)* G0 animals, our published *tol2* plasmid containing *tol2*
471 sites, the *mpeg1.1* promoter and the *cryaa:DsRed* transgenesis marker (Peterman et al., 2024)
472 was modified to insert EB3-GFP downstream of the *mpeg1.1* promoter. To amplify EB3-GFP,
473 the Addgene plasmid #190164 was used as template and amplified with the primers EB3-F and
474 EB3-R. Our previously published *mpeg1.1* promoter-containing plasmid was amplified using the
475 primers mpeg1.1_V_F ' and mpeg1.1_V_R. Gibson assembly was used to construct the final
476 pTol2-*mpeg1.1:EB3-GFP;cryaa:DsRed* plasmid. *tol2* mRNA and pTol2-*mpeg1.1:EB3-*
477 *GFP;cryaa:DsRed* plasmid DNA were injected into *Tg(mpeg1.1:mCherry)* embryos at the 1-cell

478   stage and larvae were screened for *cryaa:DsRed* expression. Positive animals were raised to
479   adulthood, where GFP expression was assessed in Langerhans cells.
480
481   To generate *Tg(actb2:h2b-mscarlet-mscarlet)hm63Tg* animals*,* Gibson assembly was used to
482   create an H2B-2x-mScarlet fusion protein by adding a linker between two copies of mScarlet
483   and fusing this to the C-terminus of human histone 2B. This was cloned into the pMTB
484   expression construct that contains the zebrafish *beta-actin 2* (*actb2*) enhancer/promoter inside
485   mini-Tol2 transposon system (Xiong et al., 2013), which was used for generating stable
486   transgenics. *tol2* mRNA and plasmid DNA were injected into AB embryos at the 1-cell stage.
487   Potential founders were screened for bright red ubiquitous fluorescence and outcrossed to
488   obtain a stable line.
489
490   ***Scale removal***
491   For scale removal, adult fish were anesthetized in system water containing 200 µg/ml buffered
492   tricaine. Individual scales were removed with forceps and placed onto 6 mm plastic dishes,
493   epidermis side up, and allowed to adhere for 30 seconds before adding L-15 medium
494   prewarmed to room temperature (22°C). Following scale removal, animals were recovered in
495   system water.
496
497   ***Scale injury assay***
498   For the epidermal scratch assay (Figures 3, 4, 5), one pair of forceps was used to assist in
499   pinning the scale down by contacting a region devoid of epidermis on the anterior scale surface.
500   A second pair introduced the scratch in the middle of the epidermis. Scratches were only used
501   for data collection if they did not extend to the edge of the scale and were oval in shape (as
502   shown by representative images in Figure 3A, B). When treating scales with pharmacological
503   agents, scales were removed, placed in L-15, and pretreated with vehicle control or
504   pharmacological agent. Nocodazole-treated (50 µM) scales were pretreated for 10 minutes,
505   nocodoazole- (50 µM) + ROCKi- (25 µM) treated scales were first treated with Y-27632 (40
506   minutes) then nocodazole (10 minutes), and paclitaxel-treated (25 µM) scales were pretreated
507   for 30 minutes. After preincubation, scales were placed under a dissecting microscope,
508   scratched, and placed under the confocal microscope for imaging.
509
510   ***Microscopy and live imaging***
511   An upright Nikon Ni-E microscope equipped with an A1R MP+ confocal scanner, a piezo *z*-drive
512   (Mad City Labs Nano-F450), and a 25× water dipping objective (1.1 NA; Nikon MRD77220) was
513   used for all experiments. Laser powers between 0.5 and 1% were used for 488 and 561 nm
514   lasers in conjunction with 521/42 and 600/45 emission filter sets for GFP and RFP channels,
515   respectively. *Z*-stacks were acquired using a resonant scanner and post-processed to remove
516   noise using the denoise.ai function in NIS-Elements.
517
518   ***Steady-state chemical treatments***
519   For nocodazole and paclitaxel treatments, scales were removed, placed onto dry 6 mm dishes,
520   and incubated in 5 ml L-15 media. Imaging commenced for at least 10 minutes before careful

521   addition of chemicals while on the microscope stage. Appropriate vehicle controls (DMSO) were
522   used at equivalent %v/v.

523

524   ***Laser-induced cell damage***
525   For laser-induced cell damage, scales were mounted as described above. Target cells at least 1
526   cell distance away from a Langerhans cell (~5-15 microns) and within the same *z*-plane were
527   located and ablated using a UGA-42 Caliburn pulsed 532 nm laser (Rapp OptoElectronic). The
528   laser was focused through a 25× objective at 4× zoom. Ablation was produced in the focal plane
529   using 15-20% power at a single point within a nucleus, firing 3 times for 3 seconds each using a
530   custom NIS-Elements macro. In the presence of nocodazole (Figure 2), scales were first
531   pretreated with nocodazole (50 µM) for 10 minutes, followed by laser-induced cell damage and
532   subsequent confocal imaging.

533

534   ***Image analysis***
535   *Dendrite metrics*
536   Dendrites were counted as microtubule positive if the ratio of EMTB-3xGFP/mCherry in the
537   dendrite was greater than 0.5. To quantify dendrite number and length in Figure 1, dendrites
538   were manually counted and measured every 10 minutes throughout the treatment time course.
539   Numbers and lengths across the time course were averaged to obtain values shown in Figure 1.

540

541   *Sholl analysis*
542   To calculate Sholl crossings, 5 timepoints from a time-lapse micrograph were selected for each
543   cell. Each cell was thresholded and the Sholl Analysis Function in the Neuroanatomy plugin in
544   ImageJ was used to calculate Sholl crossings (Arshadi et al., 2021; Ferreira et al., 2014). The
545   resulting visualization was manually inspected to ensure accuracy. The sum of the radii
546   crossings for each cell across the time points was calculated, and the percentage of total
547   crossings was summed for each condition.

548

549   *Cell motility*
550   To calculate cell motility metrics (displacement, total distance traveled, meandering index) in
551   Figure 3, cells were thresholded and tracked using the LAP algorithm in ImageJ (Ershov et al.,
552   2022; Tinevez et al., 2017). Cells were only tracked and quantified if they could be tracked
553   throughout the entire time course. Cells were excluded if their displacement was less than 10
554   microns. To quantify the meandering index for each individual cell, the displacement of that cell
555   was divided by its total distance traveled.

556

557   To calculate the cell number in wound margin in Figure 3F, a rectangular region of 150 microns
558   wide and (length of wound x 1.2) microns long was drawn around the wound. The number of
559   cells was counted for each timepoint and normalized to time 0. Cells were only counted if >50%
560   of their cell body was within the ROI. To calculate the engulfing and stretching phenotypes in
561   Figure 5, the total number of cells at 2 hours within the wound margin (rectangular region of 150
562   microns wide and (length of wound x 1.2) microns long) was counted. A second region was
563   drawn around the closing wound (as seen in Figure 5H, I). Cells were scored as engulfing if they
564   were within the wound and presenting a rounded, phagocytic phenotype. Cells were scored as

565   stretching if they extended dendrites, but not the cell body, into the wound. Frames prior to the 2

566   hour time were used as references to score if cells were morphologically changing into either of

567   these phenotypes.

568

569   *Trailing and leading edge Lifeact intensity*

570   To calculate the trailing/leading edge Lifeact-mRuby ratio in Figure 4, a set of custom ImageJ

571   macros were used. Migrating cells were thresholded and outlined over time. The outlines were

572   used as ROIs, bisected to make a trailing half and leading half, and mean Lifeact-mRuby

573   intensity in each half was quantified at each time point. The mean of means for trailing and

574   leading halves over the course of migration was calculated and the ratio of trailing/leading was

575   plotted.

576

577   *MTOC motility and positioning*

578   MTOCs were manually tracked in ImageJ in order to quantify their speed and distance from

579   phagosome (Figure 2A-G). To score MTOC decision making in Figure 5B, a decision was

580   scored as MTOC-first if the MTOC was the first structure to move past the obstacle nucleus. A

581   decision was scored nucleus-first if the nucleus preceded the MTOC. To score successful

582   navigation and navigation times in Figure 5, the difference in time between an MTOC first

583   encountering a nucleus and its successful progression past the obstacle was calculated.

584   Navigations were scored unsuccessful if the MTOC did not progress past the obstacle nucleus

585   within at least a 55 minute observation window.

586   **Statistical analysis**

587   GraphPad Prism was used to generate graphs and perform statistical analyses. At least three

588   individual biological experiments were performed unless otherwise noted. Tests used and

589   number scales or cells/ROIs are described in each figure legend.

590

591   **SUPPLEMENTAL FIGURES**

592

593
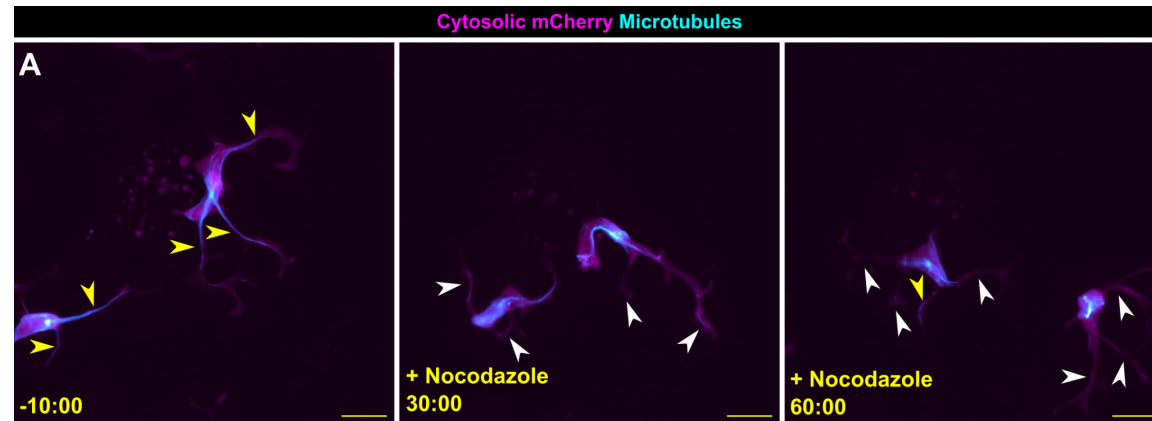
594   **Supplemental Figure 1. Confirmation of the EMTB-3xGFP reporter for tracking**
595   **microtubules. A.** Representative images from confocal time lapse microscopy of
596   *Tg(mpeg1.1:mCherry;mpeg1.1:EMTB-3xGFP)+* Langerhans cells showing effects of
597   nocodazole treatment on EMTB signal within Langerhans cells. Yellow arrowheads indicate
598   EMTB-positive dendrites, white arrowheads indicate EMTB-negative dendrites. Timestamps
599   denote mm:ss relative to the addition of nocodazole. Scale bar, 10 μm.
600

601 **SUPPLEMENTAL VIDEO LEGENDS**
602
603 **Supplemental Video 1.** Time-lapse microscopy of Langerhans cell (magenta;
604 *Tg(mpeg1.1:mCherry)*) expressing the microtubule reporter EMTB-3xGFP (cyan;
605 *Tg(mpeg1.1:EMTB-3xGFP)*). Scale bar, 10 μm.
606
607 **Supplemental Video 2.** Time-lapse microscopy of Langerhans cell (magenta;
608 *Tg(mpeg1.1:mCherry)*) expressing the plus-end microtubule reporter EB3-GFP (cyan). Scale
609 bar, 10 μm.
610
611 **Supplemental Video 3.** Time-lapse microscopy of Langerhans cells (white; *Tg(mpeg1.1:YFP)*)
612 treated with vehicle, nocodazole, or paclitaxel in steady-state conditions. Scale bar, 20 μm.
613
614 **Supplemental Video 4.** Time-lapse microscopy of a Langerhans cell (magenta;
615 *Tg(mpeg1.1:mCherry)*) MTOC during debris engulfing via tracking of EMTB-3xGFP foci
616 (*Tg(mpeg1.1:EMTB-3xGFP)*). Asterisk indicates site of keratinocyte laser ablation, white line
617 traces the MTOC motility during engulfment. Scale bar, 10 μm.
618
619 **Supplemental Video 5.** Time-lapse microscopy of Langerhans cell (white; *Tg(mpeg1.1:YFP)*)
620 engulfing cellular debris generated after laser-induced damage of keratinocytes. Cells are
621 treated with vehicle or nocodazole. Asterisk indicates site of keratinocyte laser ablation. Scale
622 bar, 10 μm.
623
624 **Supplemental Video 6.** Time-lapse microscopy of Langerhans cells (cyan;
625 *Tg(mpeg1.1:mCherry)*) reacting to epidermal wounds (epidermal cells labeled in white;
626 *Gt(ctnna1-Citrine)*). Cells are treated with vehicle or nocodazole. Scale bar, 100 μm.
627
628 **Supplemental Video 7.** Time-lapse microscopy of MTOC-labeled Langerhans cell (cyan;
629 *Tg(mpeg1.1:EMTB-3xGFP)*) navigating around obstacle nuclei (magenta;*Tg(actb2:H2B-2x-
630 mScarlet)*) in order to reach the epidermal wound. Asterisk indicates an obstacle nucleus. Scale
631 bar, 10 μm.
632
633 **Supplemental Video 8.** Time-lapse microscopy of MTOC-labeled Langerhans cell
634 (cyan;*Tg(mpeg1.1:EMTB-3xGFP)*) navigating around obstacle nuclei (magenta;*Tg(actb2:H2B-
635 2x-mScarlet)*) in order to reach the epidermal wound. Cells are treated with vehicle or paclitaxel.
636 Asterisk indicates an obstacle nucleus. Scale bar, 10 μm.
637
638

REFERENCES

Alraies, Z., C.A. Rivera, M.-G. Delgado, D. Sanséau, M. Maurin, R. Amadio, G. Maria Piperno, G. Dunsmore, A. Yatim, L. Lacerda Mariano, A. Kniazeva, V. Calmettes, P.J. Sáez, A. Williart, H. Popard, M. Gratia, O. Lamiable, A. Moreau, Z. Fusilier, L. Crestey, B. Albaud, P. Legoix, A.S. Dejean, A.-L. Le Dorze, H. Nakano, D.N. Cook, T. Lawrence, N. Manel, F. Benvenuti, F. Ginhoux, H.D. Moreau, G. P. F. Nader, M. Piel, and A.-M. Lennon-Duménil. 2024. Cell shape sensing licenses dendritic cells for homeostatic migration to lymph nodes. *Nat Immunol*. 25:1193–1206. doi:10.1038/s41590-024-01856-3.

Aman, A.J., and D.M. Parichy. 2024. Anatomy, development and regeneration of zebrafish elasmoid scales. *Dev Biol*. 510:1–7. doi:10.1016/j.ydbio.2024.03.001.

Ambravaneswaran, V., I.Y. Wong, A.J. Aranyosi, M. Toner, and D. Irimia. 2010. Directional decisions during neutrophil chemotaxis inside bifurcating channels. *Integrative Biology*. 2:639–647. doi:10.1039/c0ib00011f.

Arshadi, C., U. Günther, M. Eddison, K.I.S. Harrington, and T.A. Ferreira. 2021. SNT: a unifying toolbox for quantification of neuronal anatomy. *Nat Methods*. 18:374–377. doi:10.1038/s41592-021-01105-7.

Athlin, L., L. Domellof, and B.O. Norberg. 1986. The phagocytosis of yeast cells by monocytes: effects of colchicine, beta-lumicolchicine, and gamma-lumicolchicine. *Lymphology*. 19:130–135.

Bacci, S., T. Nakamura, and J. Wayne Streilein. 1996. Failed Antigen Presentation After UVB Radiation Correlates With Modifications of Langerhans Cell Cytoskeleton. *Journal of Investigative Dermatology*. 107:838–843. doi:10.1111/1523-1747.ep12330994.

Barros-Becker, F., P.-Y. Lam, R. Fisher, and A. Huttenlocher. 2017. Live imaging reveals distinct modes of neutrophil and macrophage migration within interstitial tissues. *Journal of Cell Science*. 130:3801–3808. doi:10.1242/jcs.206128.

Bindels, D.S., L. Haarbosch, L. van Weeren, M. Postma, K.E. Wiese, M. Mastop, S. Aumonier, G. Gotthard, A. Royant, M.A. Hink, and T.W.J. Gadella. 2017. mScarlet: a bright monomeric red fluorescent protein for cellular imaging. *Nat Methods*. 14:53–56. doi:10.1038/nmeth.4074.

Brand, A., A.-H. Hovav, and B.E. Clausen. 2023. Langerhans cells in the skin and oral mucosa: Brothers in arms? *European Journal of Immunology*. 53:2149499. doi:10.1002/eji.202149499.

Ching, K., J.T. Wang, and T. Stearns. 2022. Long-range migration of centrioles to the apical surface of the olfactory epithelium. *eLife*. 11:e74399. doi:10.7554/eLife.74399.

Dee, C.T., R.T. Nagaraju, E.I. Athanasiadis, C. Gray, L. Fernandez del Ama, S.A. Johnston, C.J. Secombes, A. Cvejic, and A.F.L. Hurlstone. 2016. CD4-Transgenic Zebrafish Reveal Tissue-Resident Th2- and Regulatory T Cell–like Populations and Diverse Mononuclear Phagocytes. *The Journal of Immunology*. 197:3520–3530. doi:10.4049/jimmunol.1600959.

Delgado, M.-G., A.-K. Burkhart, J. Villar, R. Amadio, V.S. Racz, D. Sanséau, N.D. Silva, L.L. Mariano, A. Shmakova, A. Chipont, M.S. Roman, G. Bracchetti, V. Calmettes, Z. Alraies, M. Maurin, A. Dauphin, C. Guerin, F. Ginhoux, N. Manel, D. Fachinetti, F. Benvenuti, S. Iden, and A.-M. Lennon-Duménil. 2024. The Arp2/3 complex maintains genome integrity and survival of epidermal Langerhans cells. 2024.12.27.630538. doi:10.1101/2024.12.27.630538.

Delgado, M.-G., and A.-M. Lennon-Duménil. 2022. How cell migration helps immune sentinels. *Front. Cell Dev. Biol.* 10. doi:10.3389/fcell.2022.932472.

Dogterom, M., and G.H. Koenderink. 2019. Actin-microtubule crosstalk in cell biology. *Nat Rev Mol Cell Biol*. 20:38–54. doi:10.1038/s41580-018-0067-1.

689   Ellett, F., L. Pase, J.W. Hayman, A. Andrianopoulos, and G.J. Lieschke. 2011. mpeg1 promoter
690   transgenes direct macrophage-lineage expression in zebrafish. *Blood*. 117:e49-56.
691   doi:10.1182/blood-2010-10-314120.
692   Eng, E.W., A. Bettio, J. Ibrahim, and R.E. Harrison. 2007. MTOC reorientation occurs during
693   FcgammaR-mediated phagocytosis in macrophages. *Mol Biol Cell*. 18:2389–2399.
694   doi:10.1091/mbc.e06-12-1128.
695   Ershov, D., M.-S. Phan, J.W. Pylvänäinen, S.U. Rigaud, L. Le Blanc, A. Charles-Orszag, J.R.W.
696   Conway, R.F. Laine, N.H. Roy, D. Bonazzi, G. Duménil, G. Jacquemet, and J.-Y.
697   Tinevez. 2022. TrackMate 7: integrating state-of-the-art segmentation algorithms into
698   tracking pipelines. *Nat Methods*. 19:829–832. doi:10.1038/s41592-022-01507-1.
699   Etienne-Manneville, S. 2013. Microtubules in Cell Migration. *Annu. Rev. Cell Dev. Biol.* 29:471–
700   499. doi:10.1146/annurev-cellbio-101011-155711.
701   Faire, K., C.M. Waterman-Storer, D. Gruber, D. Masson, E.D. Salmon, and J.C. Bulinski. 1999.
702   E-MAP-115 (ensconsin) associates dynamically with microtubules in vivo and is not a
703   physiological modulator of microtubule dynamics. *J Cell Sci*. 112 (Pt 23):4243–4255.
704   doi:10.1242/jcs.112.23.4243.
705   Fernandes, N.R.J., N.S. Reilly, D.C. Schrock, D.C. Hocking, P.W. Oakes, and D.J. Fowell.
706   2020. CD4+ T Cell Interstitial Migration Controlled by Fibronectin in the Inflamed Skin.
707   *Front. Immunol.* 11. doi:10.3389/fimmu.2020.01501.
708   Ferreira, T.A., A.V. Blackman, J. Oyrer, S. Jayabal, A.J. Chung, A.J. Watt, P.J. Sjöström, and
709   D.J. van Meyel. 2014. Neuronal morphometry directly from bitmap images. *Nat Methods*.
710   11:982–984. doi:10.1038/nmeth.3125.
711   Ganguly, A., H. Yang, and F. Cabral. 2011. Class III β-Tubulin Counteracts the Ability of
712   Paclitaxel to Inhibit Cell Migration. *Oncotarget*. 2:368–377. doi:10.18632/oncotarget.250.
713   Guerrero, P.A.L., J.P. Rasmussen, and E. Peterman. 2024. Calcium dynamics of skin-resident
714   macrophages during homeostasis and tissue injury. *MBoC*. mbc.E24-09-0420.
715   doi:10.1091/mbc.E24-09-0420.
716   Harada, Y., Y. Tanaka, M. Terasawa, M. Pieczyk, K. Habiro, T. Katakai, K. Hanawa-Suetsugu,
717   M. Kukimoto-Niino, T. Nishizaki, M. Shirouzu, X. Duan, T. Uruno, A. Nishikimi, F.
718   Sanematsu, S. Yokoyama, J.V. Stein, T. Kinashi, and Y. Fukui. 2012. DOCK8 is a
719   Cdc42 activator critical for interstitial dendritic cell migration during immune responses.
720   *Blood*. 119:4451–4461. doi:10.1182/blood-2012-01-407098.
721   He, S., J. Chen, Y. Jiang, Y. Wu, L. Zhu, W. Jin, C. Zhao, T. Yu, T. Wang, S. Wu, X. Lin, J.Y.
722   Qu, Z. Wen, W. Zhang, and J. Xu. 2018. Adult zebrafish Langerhans cells arise from
723   hematopoietic stem/progenitor cells. *eLife*. 7:e36131. doi:10.7554/eLife.36131.
724   Heck, J.N., S.M. Ponik, M.G. Garcia-Mendoza, C.A. Pehlke, D.R. Inman, K.W. Eliceiri, and P.J.
725   Keely. 2012. Microtubules regulate GEF-H1 in response to extracellular matrix stiffness.
726   *MBoC*. 23:2583–2592. doi:10.1091/mbc.e11-10-0876.
727   Hui, S.P., D.Z. Sheng, K. Sugimoto, A. Gonzalez-Rajal, S. Nakagawa, D. Hesselson, and K.
728   Kikuchi. 2017. Zebrafish Regulatory T Cells Mediate Organ-Specific Regenerative
729   Programs. *Developmental Cell*. 43:659-672.e5. doi:10.1016/j.devcel.2017.11.010.
730   Ishizaki, T., M. Uehata, I. Tamechika, J. Keel, K. Nonomura, M. Maekawa, and S. Narumiya.
731   2000. Pharmacological Properties of Y-27632, a Specific Inhibitor of Rho-Associated
732   Kinases. *Mol Pharmacol*. 57:976–983.
733   Kashyap, A.S., L. Fernandez-Rodriguez, Y. Zhao, G. Monaco, M.P. Trefny, N. Yoshida, K.
734   Martin, A. Sharma, N. Olieric, P. Shah, M. Stanczak, N. Kirchhammer, S.-M. Park, S.
735   Wieckowski, H. Laubli, R. Zagani, B. Kasenda, M.O. Steinmetz, H.-C. Reinecker, and A.
736   Zippelius. 2019. GEF-H1 Signaling upon Microtubule Destabilization Is Required for
737   Dendritic Cell Activation and Specific Anti-tumor Responses. *Cell Reports*. 28:3367-
738   3380.e8. doi:10.1016/j.celrep.2019.08.057.
739   Kobayashi, I., J. Kobayashi-Sun, A.D. Kim, C. Pouget, N. Fujita, T. Suda, and D. Traver. 2014.

Jam1a-Jam2a interactions regulate haematopoietic stem cell fate through Notch signalling. *Nature*. 512:319–23. doi:10.1038/nature13623.

Kopf, A., J. Renkawitz, R. Hauschild, I. Girkontaite, K. Tedford, J. Merrin, O. Thorn-Seshold, D. Trauner, H. Häcker, K.-D. Fischer, E. Kiermaier, and M. Sixt. 2020. Microtubules control cellular shape and coherence in amoeboid migrating cells. *Journal of Cell Biology*. 219. doi:10.1083/jcb.201907154.

Krendel, M., F.T. Zenke, and G.M. Bokoch. 2002. Nucleotide exchange factor GEF-H1 mediates cross-talk between microtubules and the actin cytoskeleton. *Nat Cell Biol*. 4:294–301. doi:10.1038/ncb773.

Kroll, J., R. Hauschild, A. Kuznetcov, K. Stefanowski, M.D. Hermann, J. Merrin, L. Shafeek, A. Müller-Taubenberger, and J. Renkawitz. 2023. Adaptive pathfinding by nucleokinesis during amoeboid migration. *The EMBO Journal*. 42:e114557. doi:10.15252/embj.2023114557.

Kubo, A., K. Nagao, M. Yokouchi, H. Sasaki, and M. Amagai. 2009. External antigen uptake by Langerhans cells with reorganization of epidermal tight junction barriers. *Journal of Experimental Medicine*. 206:2937–2946. doi:10.1084/jem.20091527.

Lämmermann, T., J. Renkawitz, X. Wu, K. Hirsch, C. Brakebusch, and M. Sixt. 2009. Cdc42-dependent leading edge coordination is essential for interstitial dendritic cell migration. *Blood*. 113:5703–5710. doi:10.1182/blood-2008-11-191882.

Larsen, C.P., R.M. Steinman, M. Witmer-Pack, D.F. Hankins, P.J. Morris, and J.M. Austyn. 1990. Migration and maturation of Langerhans cells in skin transplants and explants. *Journal of Experimental Medicine*. 172:1483–1493. doi:10.1084/jem.172.5.1483.

Lin, X., Q. Zhou, C. Zhao, G. Lin, J. Xu, and Z. Wen. 2019. An Ectoderm-Derived Myeloid-like Cell Population Functions as Antigen Transporters for Langerhans Cells in Zebrafish Epidermis. *Developmental Cell*. 49:605-617.e5. doi:10.1016/j.devcel.2019.03.028.

Maître, J.-L., H. Berthoumieux, S.F.G. Krens, G. Salbreux, F. Jülicher, E. Paluch, and C.-P. Heisenberg. 2012. Adhesion functions in cell sorting by mechanically coupling the cortices of adhering cells. *Science*. 338:253–256. doi:10.1126/science.1225399.

Martin, K., P. Müller, J. Schreiner, S.S. Prince, D. Lardinois, V.A. Heinzelmann-Schwarz, D.S. Thommen, and A. Zippelius. 2014. The microtubule-depolymerizing agent ansamitocin P3 programs dendritic cells toward enhanced anti-tumor immunity. *Cancer Immunol Immunother*. 63:925–938. doi:10.1007/s00262-014-1565-4.

Meiring, J.C.M., B.I. Shneyer, and A. Akhmanova. 2020. Generation and regulation of microtubule network asymmetry to drive cell polarity. *Current Opinion in Cell Biology*. 62:86–95. doi:10.1016/j.ceb.2019.10.004.

Möller, K., M. Brambach, A. Villani, E. Gallo, D. Gilmour, and F. Peri. 2022. A role for the centrosome in regulating the rate of neuronal efferocytosis by microglia in vivo. *eLife*. 11:e82094. doi:10.7554/eLife.82094.

Nestle, F.O., P. Di Meglio, J.-Z. Qin, and B.J. Nickoloff. 2009. Skin immune sentinels in health and disease. *Nat Rev Immunol*. 9:679–691. doi:10.1038/nri2622.

Nishibu, A., B.R. Ward, J.V. Jester, H.L. Ploegh, M. Boes, and A. Takashima. 2006. Behavioral Responses of Epidermal Langerhans Cells In Situ to Local Pathological Stimuli. *Journal of Investigative Dermatology*. 126:787–796. doi:10.1038/sj.jid.5700107.

Nombela-Arrieta, C., T.R. Mempel, S.F. Soriano, I. Mazo, M.P. Wymann, E. Hirsch, C. Martínez-A., Y. Fukui, U.H. von Andrian, and J.V. Stein. 2007. A central role for DOCK2 during interstitial lymphocyte motility and sphingosine-1-phosphate–mediated egress. *Journal of Experimental Medicine*. 204:497–510. doi:10.1084/jem.20061780.

Park, E.J., A. Peixoto, Y. Imai, A. Goodarzi, G. Cheng, C.V. Carman, U.H. von Andrian, and M. Shimaoka. 2010. Distinct roles for LFA-1 affinity regulation during T-cell adhesion, diapedesis, and interstitial migration in lymph nodes. *Blood*. 115:1572–1581. doi:10.1182/blood-2009-08-237917.

791 Park, S., C. Matte-Martone, D.G. Gonzalez, E.A. Lathrop, D.P. May, C.M. Pineda, J.L. Moore,
792   J.D. Boucher, E. Marsh, A. Schmitter-Sánchez, K. Cockburn, O. Markova, Y. Bellaïche,
793   and V. Greco. 2021. Skin-resident immune cells actively coordinate their distribution with
794   epidermal cells during homeostasis. *Nat Cell Biol*. 23:476–484. doi:10.1038/s41556-021-
795   00670-5.
796 Peña, O.A., and P. Martin. 2024. Cellular and molecular mechanisms of skin wound healing.
797   *Nat Rev Mol Cell Biol*. 1–18. doi:10.1038/s41580-024-00715-1.
798 Peterman, E., E.J.A. Quitevis, E.C. Black, E.C. Horton, R.L. Aelmore, E. White, A. Sagasti, and
799   J.P. Rasmussen. 2023. Zebrafish cutaneous injury models reveal Langerhans cells
800   engulf axonal debris in adult epidermis. *Disease Models & Mechanisms*. dmm.049911.
801   doi:10.1242/dmm.049911.
802 Peterman, E., E.J.A. Quitevis, C.E.A. Goo, and J.P. Rasmussen. 2024. Rho-associated kinase
803   regulates Langerhans cell morphology and responsiveness to tissue damage. *Cell
804   Reports*. 43:114208. doi:10.1016/j.celrep.2024.114208.
805 Renkawitz, J., A. Kopf, J. Stopp, I. de Vries, M.K. Driscoll, J. Merrin, R. Hauschild, E.S. Welf, G.
806   Danuser, R. Fiolka, and M. Sixt. 2019. Nuclear positioning facilitates amoeboid migration
807   along the path of least resistance. *Nature*. 568:546–550. doi:10.1038/s41586-019-1087-
808   5.
809 Renkawitz, J., A. Reversat, A. Leithner, J. Merrin, and M. Sixt. 2018. Chpater 5 - Micro-
810   engineered "pillar forests" to study cell migration in complex but controlled 3D
811   environments. *In* Methods in Cell Biology. M. Piel, D. Fletcher, and J. Doh, editors.
812   Academic Press. 79–91.
813 Robertson, T.F., Y. Hou, J. Schrope, S. Shen, J. Rindy, J.-D. Sauer, H.Q. Dinh, and A.
814   Huttenlocher. 2023. A tessellated lymphoid network provides whole-body T cell
815   surveillance in zebrafish. *Proceedings of the National Academy of Sciences*.
816   120:e2301137120. doi:10.1073/pnas.2301137120.
817 Roca, F.J., and L. Ramakrishnan. 2013. TNF Dually Mediates Resistance and Susceptibility to
818   Mycobacteria via Mitochondrial Reactive Oxygen Species. *Cell*. 153:521–534.
819   doi:10.1016/j.cell.2013.03.022.
820 Schiff, P.B., J. Fant, and S.B. Horwitz. 1979. Promotion of microtubule assembly in vitro by
821   taxol. *Nature*. 277:665–667. doi:10.1038/277665a0.
822 Schiff, P.B., and S.B. Horwitz. 1980. Taxol stabilizes microtubules in mouse fibroblast cells.
823   *Proceedings of the National Academy of Sciences*. 77:1561–1565.
824   doi:10.1073/pnas.77.3.1561.
825 Schindelin, J., I. Arganda-Carreras, E. Frise, V. Kaynig, M. Longair, T. Pietzsch, S. Preibisch, C.
826   Rueden, S. Saalfeld, B. Schmid, J.-Y. Tinevez, D.J. White, V. Hartenstein, K. Eliceiri, P.
827   Tomancak, and A. Cardona. 2012. Fiji: an open-source platform for biological-image
828   analysis. *Nature Methods*. 9:676–82. doi:10.1038/nmeth.2019.
829 Stepanova, T., J. Slemmer, C.C. Hoogenraad, G. Lansbergen, B. Dortland, C.I.D. Zeeuw, F.
830   Grosveld, G. van Cappellen, A. Akhmanova, and N. Galjart. 2003. Visualization of
831   Microtubule Growth in Cultured Neurons via the Use of EB3-GFP (End-Binding Protein
832   3-Green Fluorescent Protein). *J. Neurosci.* 23:2655–2664. doi:10.1523/JNEUROSCI.23-
833   07-02655.2003.
834 Tabdanov, E.D., N.J. Rodríguez-Merced, A.X. Cartagena-Rivera, V.V. Puram, M.K. Callaway,
835   E.A. Ensminger, E.J. Pomeroy, K. Yamamoto, W.S. Lahr, B.R. Webber, B.S. Moriarity,
836   A.S. Zhovmer, and P.P. Provenzano. 2021. Engineering T cells to enhance 3D migration
837   through structurally and mechanically complex tumor microenvironments. *Nat Commun*.
838   12:2815. doi:10.1038/s41467-021-22985-5.
839 Tinevez, J.-Y., N. Perry, J. Schindelin, G.M. Hoopes, G.D. Reynolds, E. Laplantine, S.Y.
840   Bednarek, S.L. Shorte, and K.W. Eliceiri. 2017. TrackMate: An open and extensible
841   platform for single-particle tracking. *Methods*. 115:80–90.

842   doi:10.1016/j.ymeth.2016.09.016.

843   Trinh, L.A., T. Hochgreb, M. Graham, D. Wu, F. Ruf-Zamojski, C.S. Jayasena, A. Saxena, R.
844   Hawk, A. Gonzalez-Serricchio, A. Dixson, E. Chow, C. Gonzales, H.-Y. Leung, I.
845   Solomon, M. Bronner-Fraser, S.G. Megason, and S.E. Fraser. 2011. A versatile gene
846   trap to visualize and interrogate the function of the vertebrate proteome. *Genes Dev*.
847   25:2306–2320. doi:10.1101/gad.174037.111.

848   Tweedy, L., P.A. Thomason, P.I. Paschke, K. Martin, L.M. Machesky, M. Zagnoni, and R.H.
849   Insall. 2020. Seeing around corners: Cells solve mazes and respond at a distance using
850   attractant breakdown. *Science*. 369:eaay9792. doi:10.1126/science.aay9792.

851   Vine, E.E., P.J. Austin, T.R. O'Neil, N. Nasr, K.M. Bertram, A.L. Cunningham, and A.N. Harman.
852   2024. Epithelial dendritic cells vs. Langerhans cells: Implications for mucosal vaccines.
853   *Cell Reports*. 43:113977. doi:10.1016/j.celrep.2024.113977.

854   Walter, R.J., R.D. Berlin, J.R. Pfeiffer, and J.M. Oliver. 1980. Polarization of endocytosis and
855   receptor topography on cultured macrophages. *The Journal of cell biology*. 86:199–211.
856   doi:10.1083/jcb.86.1.199.

857   Wang, B., P. Amerio, and D.N. Sauder. 1999a. Role of cytokines in epidermal Langerhans cell
858   migration. *Journal of Leukocyte Biology*. 66:33–39. doi:10.1002/jlb.66.1.33.

859   Wang, B., L. Zhuang, H. Fujisawa, G.A. Shinder, C. Feliciani, G.M. Shivji, H. Suzuki, P. Amerio,
860   P. Toto, and D.N. Sauder. 1999b. Enhanced Epidermal Langerhans Cell Migration in IL-
861   10 Knockout Mice1. *The Journal of Immunology*. 162:277–283.
862   doi:10.4049/jimmunol.162.1.277.

863   Wang, X., C.C. Decker, L. Zechner, S. Krstin, and M. Wink. 2019. In vitro wound healing of
864   tumor cells: inhibition of cell migration by selected cytotoxic alkaloids. *BMC
865   Pharmacology and Toxicology*. 20:4. doi:10.1186/s40360-018-0284-4.

866   Wang, Z.-C., Y.-Y. Hu, X.Z. Shen, and W.-Q. Tan. 2024. Absence of Langerhans cells resulted
867   in over-influx of neutrophils and increased bacterial burden in skin wounds. *Cell Death
868   Dis*. 15:1–14. doi:10.1038/s41419-024-07143-1.

869   Wasko, R., K. Bridges, R. Pannone, I. Sidhu, Y. Xing, S. Naik, K. Miller-Jensen, and V. Horsley.
870   2022. Langerhans cells are essential components of the angiogenic niche during murine
871   skin repair. *Dev Cell*. 57:2699-2713.e5. doi:10.1016/j.devcel.2022.11.012.

872   Weber, M., R. Hauschild, J. Schwarz, C. Moussion, I. de Vries, D.F. Legler, S.A. Luther, T.
873   Bollenbach, and M. Sixt. 2013. Interstitial Dendritic Cell Guidance by Haptotactic
874   Chemokine Gradients. *Science*. 339:328–332. doi:10.1126/science.1228456.

875   Wilson, K., A. Lewalle, M. Fritzsche, R. Thorogate, T. Duke, and G. Charras. 2013. Mechanisms
876   of leading edge protrusion in interstitial migration. *Nat Commun*. 4:2896.
877   doi:10.1038/ncomms3896.

878   Xiong, F., A.R. Tentner, P. Huang, A. Gelas, K.R. Mosaliganti, L. Souhait, N. Rannou, I.A.
879   Swinburne, N.D. Obholzer, P.D. Cowgill, A.F. Schier, and S.G. Megason. 2013.
880   Specified neural progenitors sort to form sharp domains after noisy Shh signaling. *Cell*.
881   153:550–561. doi:10.1016/j.cell.2013.03.023.

882   Yoo, S.K., Q. Deng, P.J. Cavnar, Y.I. Wu, K.M. Hahn, and A. Huttenlocher. 2010. Differential
883   Regulation of Protrusion and Polarity by PI(3)K during Neutrophil Motility in Live
884   Zebrafish. *Developmental Cell*. 18:226–236. doi:10.1016/j.devcel.2009.11.015.

885   Yoo, S.K., P. Lam, M.R. Eichelberg, L. Zasadil, W.M. Bement, and A. Huttenlocher. 2012. The
886   role of microtubules in neutrophil polarity and migration in live zebrafish. *Journal of Cell
887   Science*. 125:5702–5710. doi:10.1242/jcs.108324.

888   Zhou, Q., C. Zhao, Z. Yang, R. Qu, Y. Li, Y. Fan, J. Tang, T. Xie, and Z. Wen. 2023. Cross-
889   organ single-cell transcriptome profiling reveals macrophage and dendritic cell
890   heterogeneity in zebrafish. *Cell Rep*. 42:112793. doi:10.1016/j.celrep.2023.112793.

891